LETTER

https://doi.org/10.1038/s41586-018-0717-7

Creation and control of multi-phonon Fock states in a bulk acoustic-wave resonator

Yiwen Chu[1,2]*, Prashanta Kharel[1,2], Taekwan Yoon[1,2], Luigi Frunzio[1,2], Peter T. Rakich[1,2] & Robert J. Schoelkopf[1,2]*

Quantum states of mechanical motion can be important resources for quantum information, metrology and studies of fundamental physics. Recent demonstrations of superconducting qubits coupled to acoustic resonators have opened up the possibility of performing quantum operations on macroscale motional modes[1–3], which can act as long-lived quantum memories or transducers. In addition, they can potentially be used to test decoherence mechanisms in macroscale objects and other modifications to standard quantum theory[4,5]. Many of these applications call for the ability to create and characterize complex quantum states, such as states with a well defined phonon number, also known as phonon Fock states. Such capabilities require fast quantum operations and long coherence times of the mechanical mode. Here we demonstrate the controlled generation of multi-phonon Fock states in a macroscale bulk acoustic-wave resonator. We also perform Wigner tomography and state reconstruction to highlight the quantum nature of the prepared states[6]. These demonstrations are made possible by the long coherence times of our acoustic resonator and our ability to selectively couple a superconducting qubit to individual phonon modes. Our work shows that circuit quantum acoustodynamics[7] enables sophisticated quantum control of macroscale mechanical objects and opens up the possibility of using acoustic modes as quantum resources.

Light and sound are two examples of familiar wave phenomena in the classical world. Until now, the field of quantum optics has extensively demonstrated the particle nature of light in quantum mechanics through the study of single photons and other non-Gaussian electromagnetic states. The concept of particles of sound, or phonons, is used widely in solid state physics. However, the ability to create states of individual phonons has only been demonstrated in a few instances[1,3,8], whereas the complete quantum tomography of such states has only been achieved in a single trapped ion[6]. This disparity between electromagnetic and acoustic degrees of freedom is largely due to sound propagating inside the complex and potentially lossy environment of a massive material, rather than in vacuum. As a result, an open question remains: is it feasible to control and measure complex quantum states in the motion of a macroscale solid-state object, or what we usually think of as sound, analogously to what has been done with light?

The relatively new field of quantum acoustics attempts to answer this question using a variety of optomechanical and electromechanical systems[1,2,7,9–13], and one particularly promising approach is circuit quantum acoustodynamics (QAD)[1,2,7,13]. In analogy to circuit quantum electrodynamics (QED), circuit QAD uses superconducting quantum circuits that operate at microwave frequencies to manipulate and measure mechanical resonators. Circuit QAD takes advantage of the strong interactions between mechanics and electromagnetism enabled by, for example, piezoelectricity. It also incorporates the nonlinearity provided by the Josephson junction, which is a crucial ingredient for creating non-Gaussian states of motion. In turn, the ability to create these states makes mechanical resonators useful as resources in quantum circuits, offering capabilities beyond those of electromagnetic resonators. For example, mechanical transduction is a promising method for transferring quantum information between microwave circuits and other systems, such as optical light or spin qubits[14,15]. Owing to the difference between the speeds of sound and light, an acoustic resonator is much more compact and well isolated than an electromagnetic one at the same frequency and provides many more independent modes that are individually addressable by a superconducting qubit. Such an architecture is desirable for simulating many-body quantum systems[2,16] and provides a highly hardware-efficient way of storing, protecting and manipulating quantum information using bosonic encodings[17,18]. These examples show that by repurposing the toolbox of circuit QED through the similarities between light and sound, circuit QAD allows us to make use of the important differences between these quantum degrees of freedom. However, in order to access this toolbox, we first need to demonstrate that a circuit QAD system can be engineered to have the necessary mode structure, strong enough interactions and sufficient quantum coherence to create and characterize quantum states of motion.

In this work, we experimentally prepare and perform full quantum tomography on Fock states of phonons and their superpositions inside a high-overtone bulk acoustic-wave resonator (HBAR). This is enabled by a robust new flip-chip device geometry that couples a superconducting transmon qubit to the HBAR. This geometry allows us to optimize the design of the acoustic resonator and the qubit separately to extend phonon coherence while enhancing the selectivity of the coupling to a single mode. The combination of these improvements leads to a device that is deeper in the strong-coupling regime of circuit QAD, which is necessary for the generation and manipulation of more complex quantum states. We note that a similar demonstration using a superconducting qubit and surface acoustic waves has been recently reported[19].

We now describe the motivation behind the design of our circuit QAD system in more detail. Figure 1a shows a schematic of our device, which we call the ħBAR. The first important difference from our previous device[3] is the flip-chip geometry, where the qubit and acoustic resonator are now on separate sapphire chips[19]. This simplifies the fabrication procedure and increases the yield of successful devices (see Supplementary Information) while allowing qubits and acoustic resonators to be individually tested before assembly. Second, the ħBAR incorporates a plano-convex acoustic resonator that is fabricated using a simple, robust method and supports stable, transversely confined acoustic modes (see Supplementary Information). Because the measured acoustic lifetime in the previous unstable resonator geometry[3] was consistent with being limited by diffraction loss, this modification to our device could considerably improve phonon coherence. Another important requirement is the ability to selectively couple the qubit to a single acoustic mode. This is partly achieved by the plano-convex resonator design, which allows us to control the frequency spacing between transverse modes. To further increase mode selectivity, the third improvement is the addition of an optimized transduction electrode to the qubit. The electrode was designed to match the strain profile of the fundamental Gaussian transverse mode of the acoustic resonator (see Supplementary Information). We point out that even though the acoustic resonator is not in physical contact with the electrode, the

[1]Department of Applied Physics, Yale University, New Haven, CT, USA. [2]Yale Quantum Institute, Yale University, New Haven, CT, USA. *e-mail: yiwen.chu@yale.edu; robert.schoelkopf@yale.edu

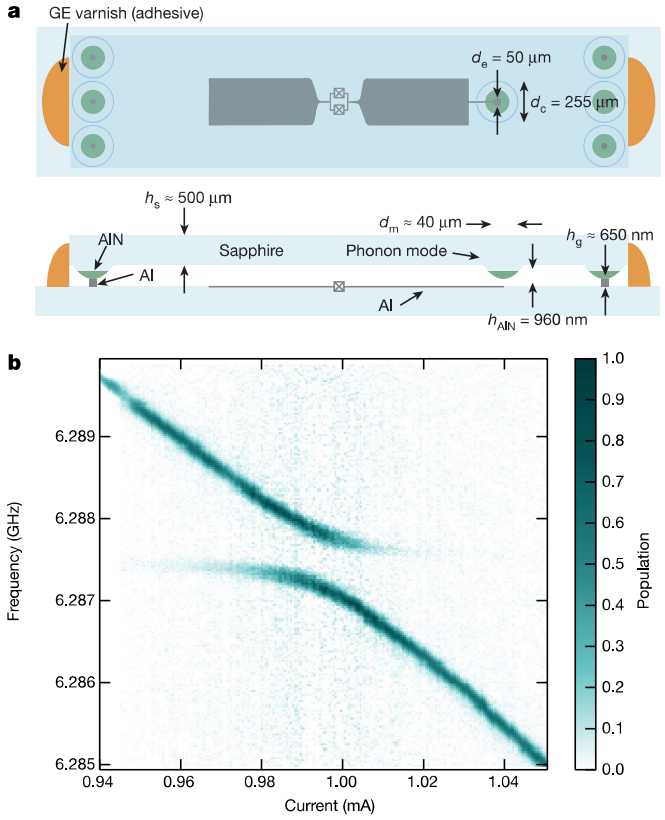

Fig. 1 | The ħBAR device and strong qubit–phonon coupling. a, Top-view (top) and side-view (bottom) schematics of the ħBAR device (not to scale). The chip containing the acoustic resonator has six nominally identical resonators on its edges, with Al (grey) spacers deposited on them. The measured thickness of the Al spacer between the qubit and acoustic resonator (h_g) is shown, but the actual spacing may be larger owing to imperfections in the flip-chip assembly. Other dimensions indicated are the diameters of the transducer electrode (d_e), curved resonator surface (d_c) and acoustic-mode waist (d_m), along with the thicknesses of the AlN (h_{AlN}; green) and sapphire substrate (h_s; blue). **b**, Spectroscopy results of the transmon qubit near the l_1 acoustic mode, measured while varying the current in an external coil used to flux-tune the qubit frequency.

electric field of the qubit extends across the gap between the two chips and through the AlN film, thus allowing piezoelectric transduction.

We now experimentally show that the new design does indeed lead to improvements in the electro-mechanical coupling, acoustic-mode spectrum and coherence of our device. As in our previous work, the ħBAR is measured using a standard circuit QED setup that allows flux-tuning of the qubit frequency using an externally applied magnetic field. Figure 1b shows qubit spectroscopy results near the $l = l_1$ and $m, n = 0$ mode of the ħBAR, which reveal a single distinct anticrossing feature. Here l is the longitudinal mode number and m, n are the mode numbers of the Hermite–Gaussian-like transverse modes. $l_1 \approx 466$ corresponds to the highest-frequency longitudinal mode that is fully within the tunable range of the qubit, as indicated in Fig. 2, where we investigate the mode structure of the ħBAR over several longitudinal free spectral ranges. Figure 2a shows the time dynamics of the qubit–phonon interaction for different qubit frequencies, which reveals features indicative of vacuum Rabi oscillations that are spaced by the longitudinal free spectral range $\nu_{FSR} = 13.5$ MHz. Each oscillatory feature corresponds to an anticrossing similar to the one shown in Fig. 1b. The Fourier transform of the data in Fig. 2a is shown in Fig. 2b and gives a qubit–phonon coupling rate of $g_0 = 2\pi \times (350 \pm 3)$ kHz. In addition to the dominant set of oscillations corresponding to the $m, n = 0$ Gaussian modes, there are clear signatures of other acoustic modes in Fig. 2a, b, which correspond to higher-order transverse modes, as indicated by simulations (see Supplementary Information). However, the closest observable higher-order mode is about 1 MHz away from the $m, n = 0$ mode and about ten times less strongly coupled to the qubit, while all other higher-order modes are at least five times less strongly coupled. (From now on, we use only the longitudinal mode number to represent the $m, n = 0$ modes.) These results indicate that the ħBAR is a good approximation of a system in which the qubit can be tuned to interact with a single acoustic mode at a time.

We demonstrate the improvements in the coherence of our system by performing quantum operations on the phonon mode using the qubit. Using techniques described in our previous work[3], we find that the phonon mode has a lifetime of $T_1 = 64 \pm 2$ μs, a Ramsey decoherence time of $T_2 = 38 \pm 2$ μs and an echo decoherence time of $T_{2e} = 45 \pm 2$ μs. On other devices, we measured the phonon lifetime to be as long as $T_1 = 113 \pm 4$ μs. These coherence times are comparable to that of state-of-the art superconducting qubits and suggest that the plano-convex resonator design does indeed support much-longer-lived phonons. The qubit in this device has a $T_1 = 7 \pm 1$ μs, which is similar to that of our previous device. As will be discussed later, we believe that these device parameters can be further improved through modifications of the materials, fabrication procedure and device geometry.

The improvements presented above allow us to perform quantum operations on the phonon mode with a new level of sophistication, which we now illustrate by creating and measuring multi-phonon Fock states. We use a procedure for Fock state preparation that has previously only been demonstrated in electromagnetic systems[20] (Fig. 3a). The experiment begins with the qubit set to a frequency ν_0 that is detuned by $\delta = -5$ MHz from the target l_1 phonon mode at frequency ν_1. The qubit ideally starts out in the ground state $|g\rangle$, but in reality has a thermal population of 4%–8% in the excited state $|e\rangle$. The phonon modes, on the other hand, have been shown to be colder[3]. Therefore we first perform a swap operation between the qubit and the l_2 mode with frequency ν_2. This procedure effectively uses an additional acoustic mode to cool the qubit to an excited-state population of about 2%. The qubit is then excited with a π pulse and brought into resonance with the l_1 mode to transfer its energy into the acoustic resonator using a swap operation. This is repeated N times to climb up the Fock state ladder and ideally results in a state of N phonons, which is then probed by bringing the qubit and phonon to resonance for a variable time t and measuring the final qubit state. We note that this measurement procedure gives the total population in the qubit excited-state subspace of the joint system and traces over the resonator state. The resulting time dynamics of the population $p_{e,N}(t)$ for up to $N = 7$ is shown in Fig. 3b. In Fig. 3c, we plot the Fourier transform of the data in Fig. 3b. As expected, we observe oscillations with a dominant frequency of $2g_N = 2\sqrt{N}g_0$, which corresponds to the rate of energy exchange between the $|g, N\rangle$ and $|e, N-1\rangle$ states.

To characterize the states that we have created more quantitatively, we extract the population in each phonon Fock state n after performing an N-phonon preparation. We do this by first simulating the expected time traces, $p_{e,n}(t)$, assuming that the phonon mode is prepared in an ideal Fock state ranging from $n = 1$ to $n_{max} = 14$. The independently measured value of g_0, along with the qubit and phonon decay and dephasing rates, are used in the simulations. Then, the experimental data for each N (Fig. 3b) are fitted to a weighted sum of the form

$$p_{e,N}(t) = \sum_{n=1}^{n_{max}} p_{n,N} p_{e,n}(t) \quad (1)$$

where $p_{n,N}$ is then the population at $|g, n\rangle$ after performing an N-phonon preparation. The fit for each N is subject to the constraints $p_{n,N} \leq 1 \; \forall \; n$ and $\sum_{n=1}^{n_{max}} p_{n,N} \leq 1$. Finally, the population in the zero-phonon state is calculated as $p_{0,N} = 1 - \sum_{n=1}^{n_{max}} p_{n,N}$. Ideally, $p_{n,N} = \delta_{n,N}$. As shown in Fig. 3d, we observe that the resulting distribution of populations for each experiment is indeed peaked at $n = N$. However, the population in the nominally prepared state decreases with increasing N. We find that $p_{1,1} = 0.86$, which is consistent with a simple estimate that takes into account the energy decay from the one-excitation

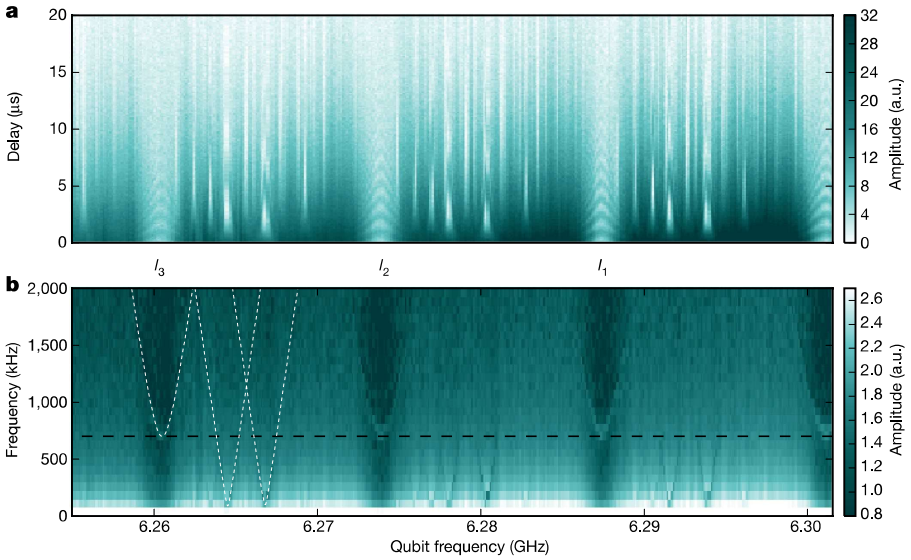

Fig. 2 | Mode structure of the ħBAR. a, Time dynamics of the qubit–phonon interaction, determined by exciting the qubit and measuring its excited-state population after a variable delay as the qubit is flux-tuned (a.u., arbitrary units). **b**, Logarithm of the Fourier transform of the data shown in **a**. The qubit frequencies shown on the horizontal axis are determined from spectroscopy data taken at each applied flux. The three highest-frequency fundamental transverse modes (m, $n = 0$) that are fully accessible by the qubit are shown and labelled with their longitudinal mode numbers. The white dashed lines indicate the hyperbolic dependence of the effective vacuum Rabi frequencies for the three most dominant modes in one free spectral range. The black dashed line indicates the value of $2g_0$ for the fundamental mode, which is at least a factor of five larger than the coupling rates to the other modes.

manifold during a swap operation, which is dominated by the qubit decay rate, and the imperfect preparation of the qubit in $|g\rangle$. For larger N values, the state preparation may be affected by additional effects, such as off-resonant driving of the phonon mode during the qubit π pulses, which could lead to excess population in the $n > N$ states. We also find that the largest source of potential error in extracting $p_{n,N}$ comes from uncertainty in the system parameters that are used in simulating $p_{e,n}(t)$. In particular, slight drifts of the qubit frequency can result in a mismatch between the value of $2g_0$ used in the simulations and the actual oscillation frequency of the vacuum Rabi data. An

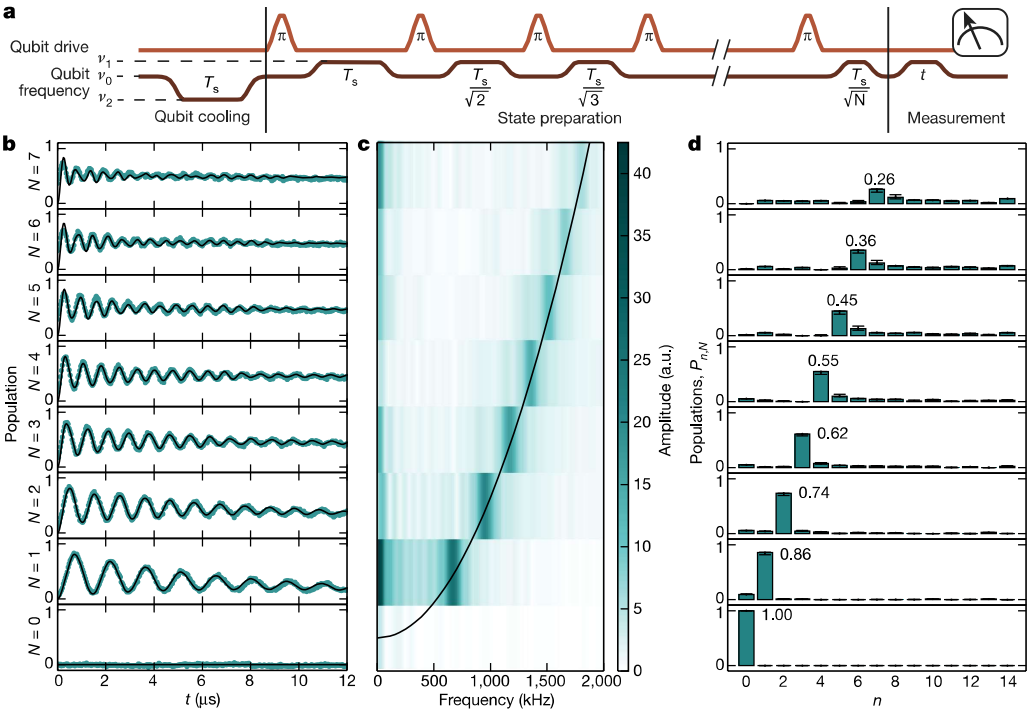

Fig. 3 | Climbing the phonon Fock state ladder. a, Pulse sequence for the generation and measurement of phonon Fock states. $T_s = \pi/2g_0$ is the duration of a swap operation in the one-excitation manifold. In the state preparation step, the duration of the kth swap is scaled to account for the coupling rate $g_k = \sqrt{k}\,g_0$ between the $|g, k\rangle$ and $|e, k-1\rangle$ states. Pulses intended to excite the qubit from $|g\rangle$ to $|e\rangle$ are labelled with 'π'. The qubit frequencies ν_0, ν_1 and ν_2 are described in the text. **b**, Qubit excited-state population after interacting with the phonon for a time t following an N-phonon preparation procedure. Black lines are fits used to extract the Fock state populations shown in **d**. **c**, Fourier transform of the data shown in **b**, obtained by subtracting the mean of each dataset in **b** and appending copies of the resultant final value to effectively smooth the Fourier transform. The black line corresponds to $2g_N$. **d**, Populations in the n Fock state, extracted from **b**. The numbers show the populations in $n = N$. Error bars indicate the result of changing the value of g_0 in the simulations of $p_{e,n}(t)$ by ±5 kHz (see main text).

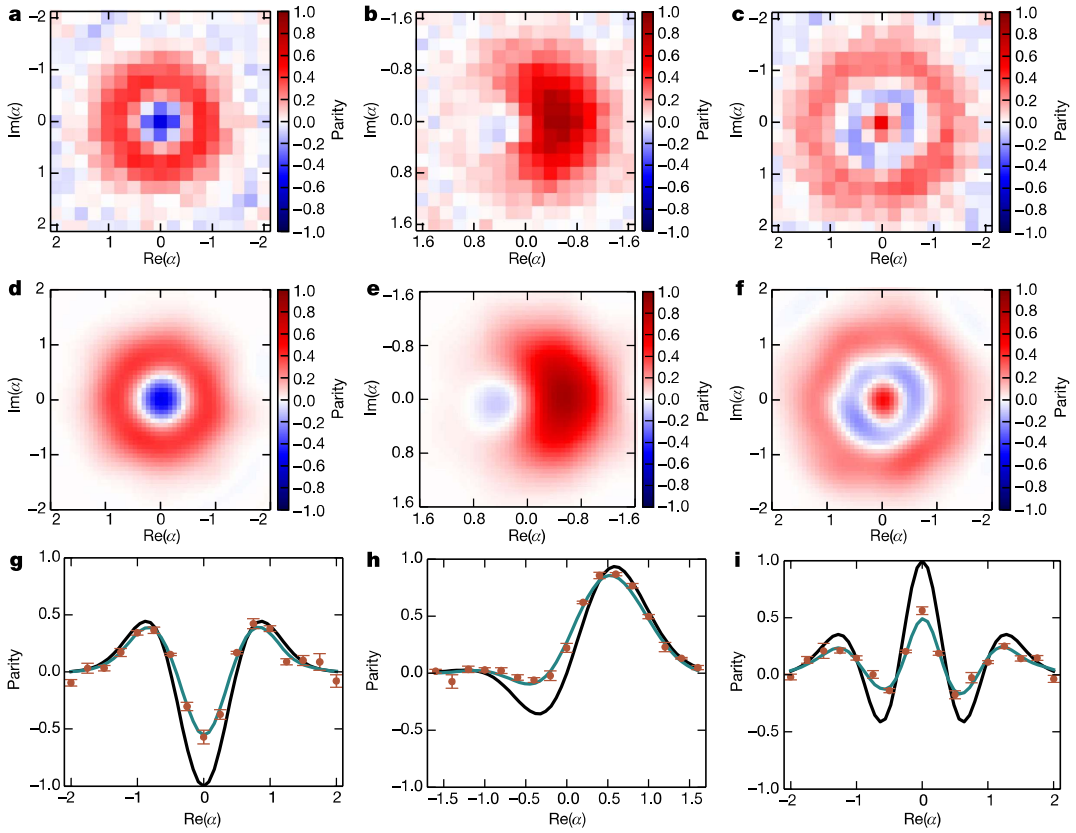

Fig. 4 | Wigner tomography of non-classical states of motion. **a–c**, Measured Wigner functions of the prepared states $|1\rangle$, $(|0\rangle + |1\rangle)/\sqrt{2}$ and $|2\rangle$. Each grid point is a separate experiment with displacement by a phase-space amplitude α. **d–f**, Wigner functions of the density matrices reconstructed from **a–c**. **g–i**, Cuts of the ideal Wigner function (black line), data (brown points) and reconstructed Wigner function (green line) along the $\mathrm{Im}(\alpha) = 0$ axis. Negative values of the Wigner function are indicators of a non-classical state of motion. The error bars are extracted in the same way as in Fig. 3d (see main text).

estimate of the effect of such miscalibrations is given by the error bars in Fig. 3d.

We now build on our ability of extracting the phonon number distribution to perform full Wigner tomography and explore the quantum nature of the prepared mechanical state. As in previous circuit QED and trapped-ion experiments[6,21], we use the definition[22]

$$P(\alpha) = \mathrm{tr}[\hat{D}(-\alpha)\rho\hat{D}(\alpha)\hat{P}] = \frac{\pi}{2}W(\alpha) \quad (2)$$

Here $P(\alpha)$ and $W(\alpha)$ are the values of the displaced parity and Wigner functions, respectively, at a phase-space amplitude α, ρ is the prepared state and $\hat{P}$ is the parity operator. From now on, we plot the values of $P(\alpha)$ for clarity, but use the terms 'displaced parity' and 'Wigner function' interchangeably. The resonator displacement $\hat{D}(\alpha)$ is implemented by a microwave pulse at the phonon frequency while the qubit is detuned at ν_0. Under these conditions, the phonon mode is still coupled to the microwave drive port, in part owing to its hybridization with the qubit. To verify this and calibrate our displacement amplitudes, we first apply a Gaussian phonon drive pulse of varying amplitude α with a root-mean-square width of 1 μs and truncated to a total length of 4 μs. We then measure the subsequent Fock state populations $p_{n,|0\rangle}(\alpha)$ and check that they agree well with the expected Poisson distributions up to an overall scaling between the amplitudes of the applied drive and the actual displacement (see Supplementary Information). We can then calculate the displaced parity for the vacuum state $|0\rangle$ using $P_{|0\rangle}(\alpha) = \sum_n (-1)^n p_{n,|0\rangle}(\alpha)$. Similarly, we can measure the displaced parity $P_\rho(\alpha)$ for an arbitrary state ρ by adding a phonon drive pulse between state preparation and measurement.

In Fig. 4, we present the results of Wigner state tomography on the nominally prepared states $|1\rangle$, $(|0\rangle + |1\rangle)/\sqrt{2}$ and $|2\rangle$. The $(|0\rangle + |1\rangle)/\sqrt{2}$ state was prepared by applying a $\pi/2$ pulse to the qubit and followed by a swap operation with the phonon mode. From the measured data shown in Fig. 4a–c, we can reconstruct the measured state using a maximum likelihood method[18] (see Supplementary Information). The Wigner functions of the reconstructed states are presented in Fig. 4d–f. Figure 4g–i shows that the reconstructed parities agree well with the raw data. The negativity of the Wigner functions clearly demonstrates the quantum nature of the states. From the reconstructed density matrices, we find that the fidelities of the prepared states to the target states are $F_{|1\rangle} = 0.87 \pm 0.01$, $F_{(|0\rangle+|1\rangle)/\sqrt{2}} = 0.94 \pm 0.01$ and $F_{|2\rangle} = 0.78 \pm 0.02$. The infidelity for all three states is dominated by excess population in the lower-number Fock states, which is an expected consequence of energy decay during state preparation and measurement (see Supplementary Information).

These results show that the quantum state of motion in a macroscale mechanical resonator can be prepared, controlled and fully characterized in a circuit QAD device. The demonstration of even more complex quantum states should be possible with further improvements of the device performance. Currently, the dominant source of loss is the qubit, and we find that its T_1 is higher when the resonator chip is either not present or rotated by 180° relative to the qubit chip. This indicates that the qubit lifetime may be limited by loss due to the AlN, which could be mitigated by using a different piezoelectric material or optimizing the device geometry to minimize the electric field in the AlN that does not contribute to transduction. The current limitations on the phonon coherence also require further investigation. The energy loss is probably dominated by surface roughness or imperfections in the fabricated geometry, whereas additional dephasing could result from thermal excitations and frequency fluctuations of the detuned qubit[23]. In addition, we can characterize the final flip-chip geometry, such as the spacing and alignment between the chips, more carefully. The assembly

process can then be modified accordingly, potentially leading to further improvements in the coupling and mode selectivity.

The next generation of devices could give us access to even more sophisticated methods for quantum control of the acoustic resonator. Our ħBAR device can almost reach the strong dispersive regime in which circuit QED systems currently operate, which would allow quantum non-demolition measurements of phonon numbers[24] and the application of more sophisticated techniques for generating arbitrary quantum states of harmonic resonators[17,25]. Furthermore, our qubit-cooling technique already takes advantage of the multimode nature of the acoustic resonator. Future experiments could, for example, demonstrate qubit-mediated interactions between multiple modes and the creation of multipartite entangled states of mechanical motion[11,12]. Recent efforts in improving the efficiency of electromechanical and optomechanical transduction with mechanical resonators could enable conversion of quantum information between the microwave and optical domains[14,26]. Beyond the use of acoustic resonators as resources for quantum information, the creation of increasingly complex quantum states in highly coherent mechanical resonators can provide insight into the question of whether quantum superpositions of massive objects are suppressed owing to mechanisms other than environmental decoherence[4,27]. In addition, the ability to apply quantum control on our large-effective-mass, high-frequency and low-thermal-occupation mechanical system may put new bounds on modifications to quantum mechanics at small length scales[28,29]. These examples suggest that the wide range of quantum acoustics demonstrations that may soon be possible with ħBAR will give rise to new quantum technologies while furthering our understanding of fundamental physics.

Data availability

The data that support the findings of this study are available from the corresponding authors upon reasonable request.

Received: 19 April 2018; Accepted: 10 September 2018;
Published online 21 November 2018.

1. O'Connell, A. D. et al. Quantum ground state and single-phonon control of a mechanical resonator. *Nature* **464**, 697–703 (2010).
2. Moores, B. A., Sletten, L. R., Viennot, J. J. & Lehnert, K. W. Cavity quantum acoustic device in the multimode strong coupling regime. *Phys. Rev. Lett.* **120**, 227701 (2018).
3. Chu, Y. et al. Quantum acoustics with superconducting qubits. *Science* **358**, 199–202 (2017).
4. Arndt, M. & Hornberger, K. Testing the limits of quantum mechanical superpositions. *Nat. Phys.* **10**, 271–277 (2014).
5. Marshall, W., Simon, C., Penrose, R. & Bouwmeester, D. Towards quantum superpositions of a mirror. *Phys. Rev. Lett.* **91**, 130401 (2003).
6. Leibfried, D. et al. Experimental determination of the motional quantum state of a trapped atom. *Phys. Rev. Lett.* **77**, 4281–4285 (1996).
7. Manenti, R. et al. Circuit quantum acoustodynamics with surface acoustic waves. *Nat. Commun.* **8**, 975 (2017).
8. Riedinger, R. et al. Non-classical correlations between single photons and phonons from a mechanical oscillator. *Nature* **530**, 313–316 (2016).
9. Lee, K. C. et al. Entangling macroscopic diamonds at room temperature. *Science* **334**, 1253–1256 (2011).
10. Safavi-Naeini, A. H. et al. Squeezed light from a silicon micromechanical resonator. *Nature* **500**, 185–189 (2013).
11. Riedinger, R. et al. Remote quantum entanglement between two micromechanical oscillators. *Nature* **556**, 473–477 (2018).
12. Ockeloen-Korppi, C. F. et al. Stabilized entanglement of massive mechanical oscillators. *Nature* **556**, 478–482 (2018).
13. Gustafsson, M. V. et al. Propagating phonons coupled to an artificial atom. *Science* **346**, 207–211 (2014).
14. Andrews, R. W. et al. Bidirectional and efficient conversion between microwave and optical light. *Nat. Phys.* **10**, 321–326 (2014).
15. Schuetz, M. J. A. et al. Universal quantum transducers based on surface acoustic waves. *Phys. Rev. X* **5**, 031031 (2015).
16. Naik, R. K. et al. Random access quantum information processors using multimode circuit quantum electrodynamics. *Nat. Commun.* **8**, 1904 (2017); publisher correction 9, 172 (2018).
17. Leghtas, Z. et al. Hardware-efficient autonomous quantum memory protection. *Phys. Rev. Lett.* **111**, 120501 (2013).
18. Chou, K. S. et al. Deterministic teleportation of a quantum gate between two logical qubits. *Nature* **561**, 368–373 (2018).
19. Satzinger, K. J. et al. Quantum control of surface acoustic-wave phonons. *Nature* https://doi.org/10.1038/s41586-018-0719-5 (2018).
20. Hofheinz, M. et al. Generation of Fock states in a superconducting quantum circuit. *Nature* **454**, 310–314 (2008).
21. Hofheinz, M. et al. Synthesizing arbitrary quantum states in a superconducting resonator. *Nature* **459**, 546–549 (2009).
22. Royer, A. Wigner function as the expectation value of a parity operator. *Phys. Rev. A* **15**, 449–450 (1977).
23. Gambetta, J. et al. Qubit-photon interactions in a cavity: measurement-induced dephasing and number splitting. *Phys. Rev. A* **74**, 042318 (2006).
24. Schuster, D. I. et al. Resolving photon number states in a superconducting circuit. *Nature* **445**, 515–518 (2007).
25. Heeres, R. W. et al. Implementing a universal gate set on a logical qubit encoded in an oscillator. *Nat. Commun.* **8**, 94 (2017).
26. Kharel, P. et al. Ultra-high-Q phononic resonators on-chip at cryogenic temperatures. *APL Photonics* **3**, 066101 (2018).
27. Penrose, R. On gravity's role in quantum state reduction. *Gen. Relativ. Gravit.* **28**, 581–600 (1996).
28. Pikovski, I., Vanner, M. R., Aspelmeyer, M., Kim, M. S. & Brukner, V. Probing planck-scale physics with quantum optics. *Nat. Physics* **8**, 393–397 (2012).
29. Marin, F. et al. Gravitational bar detectors set limits to Planck-scale physics on macroscopic variables. *Nat. Phys.* **9**, 71–73 (2013).

Acknowledgements We thank M. Devoret, S. Girvin, Y. Zhang, K. Chou and V. Jain for discussions. We thank K. Silwa for providing the Josephson parametric converter amplifier. This research was supported by the US Army Research Office (W911NF-14-1-0011), ONR YIP (N00014-17-1-2514), NSF MRSEC (DMR-1119826) and the Packard Fellowship for Science and Engineering. Facility use was provided by the Yale SEAS cleanroom, the Yale West Campus Cleanroom and the Yale Institute for Nanoscience and Quantum Engineering (YINQE).

Reviewer information *Nature* thanks S. Deleglise and the other anonymous reviewer(s) for their contribution to the peer review of this work.

Author contributions Y.C. performed the experiment and analysed the data under the supervision of P.T.R. and R.J.S. Y.C., P.K. and L.F. designed and fabricated the device. P.K. and T.Y. provided experimental suggestions and theory support. Y.C., P.K., P.T.R. and R.J.S. wrote the manuscript with contributions from all authors.

Competing interests R.J.S. and L.F. are founders and equity shareholders of Quantum Circuits, Inc.

Additional information

Supplementary information is available for this paper at https://doi.org/10.1038/s41586-018-0717-7.

Correspondence and requests for materials should be addressed to Y.C. or R.J.S.